Report Summer 2009 project

Near IR spectral analysis of the young star cluster W3 in NGC 7252 and comparison with the predictions of stellar population models

Superviseur : Harald Kuntschner

Tutrice : Simona Mei

Organisme d'accueil : European Southern Observatory (ESO)

Etablissement d'origine : Université Paris 7 Diderot (UP7)

Olivier DO CAO

Contents

Acknowledgements

First of all I would like to thank my supervisor Harald Kuntschner for his kindness, for offering me the opportunity to work on such a recent field and datas, and for his endless patience in answering my large number of questions. I would also like to thank Mariya Lyubenova, former Harald's PhD student, who provided me a great help in understanding the background and who shared some of her experience in becoming an astronomer. Finally, I would like to express my gratitude to Simona Mei who permitted me to discover ESO, one of the most exciting place for astrophysical research.

Context of project

This 3 months project presents the near-IR spectral analysis of the star cluster W3 in the nearby galaxy NGC 7252 (or Arp 226), a merger remnant[1]. This work follows the recent PhD thesis Lyubenova (2009a) (hereafter L09b) and is mostly inspired by chapters 1, 2, 3 and 6. Its results are highly linked to Lyubenova (2009b) (hereafter L09a).

The story of galaxy formation and evolution is still illunderstood, so the community needs to know more about stellar populations in order to calibrate their models. We will study here the early-type galaxies through NGC 7252 and its globular star cluster W3. L09b has shown a marked disagreement between observations and the model of Maraston (2005) (hereafter M05) for intermediate-age and half solar metallicity for Globular Clusters (GCs). The main purpose of this project is to test this Simple Stellar Population Model predicting near-IR indices versus age.

We have used in this work very recent data[2] from the SINFONI spectrograph mounted on the Very Large Telescop (VLT). The Introduction sets the context of this project, while the second chapter explains how we made the observations and the analysis. The third chapter presents the results and the discussions. The last chapter will finally present the conclusions.

[1] Also called the atoms-for-peace galaxy by Eisenhower due to its shape which reminds of a Bohr's atom

[2] Proposal 383.B-0625, June-July 2009

Chapter 1

Introduction

1.1 Galaxies in the Universe

1.1.1 Hubble's classification

Edwin Hubble ordered the galaxies he saw through the telescope in a classification scheme (M. & C. J. A., 1936) (see Figure (1.1.1)). To the left hand side of his famous "tuning fork" diagram he placed the elliptical galaxies (E), ordered by increasing ellipticity. They were followed by two branches of spiral galaxies, one ordinary (S) and one with barred spirals (SB). The connecting class were the lenticular galaxies (S0). This classification scheme was initially considered to have an evolutionary meaning. The arrow of time was directing from left to the right: from almost circular ellipticals to widely open spirals. Later more sophisticated diagrams became available, based on the physical parameters of the galaxies (e.g. Kormendy & Bender (1996)). However Hubble's diagram is still the most commonly used when classifying galaxies, based on their morphology. Astronomers still call ellipticals and lenticulars as *early-type* galaxies and spirals as *late-type* galaxies.

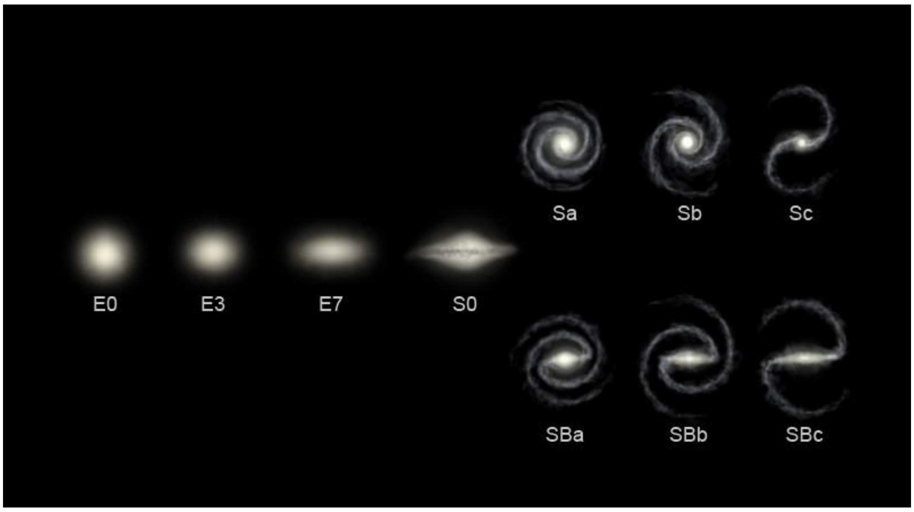

Figure 1.1.1: Hubble's classification.

There are, however, galaxies with strange appareances. It is likely that many of these structures are due to gravitational interactions or collisions between galaxies. Toomre & Toomre (1973) showed how such events could give rise to remarkable asymmetric structures[1] such as NGC 7252. Collisions between galaxies have assumed a central role in models of galaxy formation. In the most popular scenario, galaxies are built up by the process of *hierarchical clustering* in which larger galaxies are formed by the coalescence of smaller galaxies. Mergers are therefore key to understand formation and evolution of galaxies.

[1]One of the most famous picture of interacting galaxies are the Antennae caracterized by two extraordinary long tails.

1.1.2 The Merger Remnant NGC 7252

The galaxy we study is a merger remnant located at $\alpha = 22^h 20^m 44^s.8$, $\delta = -24°40'42''$. Schweizer & Seitzer (1998) measured a recession velocity relative to the Local Group of 4828 ± 2 $km.s^{-1}$, which places it at a distance of 64.4 Mpc (assuming homogeneous Hubble flow and $H_0 = 75$ $km.s^{-1}.Mpc^{-1}$, adopted throughout the present report).Hypercat[2] gives a velocity dispersion of 157 ± 20 $km.s^{-1}$. At that distance, the projected scale is $1'' = 312$ pc. The corresponding true distance modulus is $(m - M)_0 = 34.04$ and the apparent visual distance modulus is $V - M_V = 34.08$ for a Milky Way foreground extinction of $A_V = 0.05$ mag (Schweizer & Seitzer, 1998).

It has a single nucleus, a nearly round main body marked by faint surrounding loops, and two slender tails that project to 80 kpc and 130 kpc from the center (see Figure (1.1.2)). Schweizer (1982) has shown that the length of the latter divided by their velocities gives a merger age of $\sim 1Gyr$, and confirmed this result thanks to optical spectroscopy. He also gives a metallicity of about $\sim 1Z_\odot$. Five characteritics taken together suggest a recent merger of two similarly massive disk galaxies : the two tails and their opposite motions, the unusual isolation, the single nucleus and body, and the two surviving motion system of the gas. It seems to have already established an $r^{1/4}$ light distribution[3] and is more likely to evolve into an elliptical than into a lenticular.

1.1.3 The W3 Globular Cluster

W3 is the brighest star cluster in the nearby galaxy NGC 7252 and has probably been formed during the merger of its host galaxy. It has a recession velocity of 4821 ± 71 $km.s^{-1}$ (Schweizer & Seitzer, 1998) and a velocity dispersion of 45 ± 5 $km.s^{-1}$ (Maraston et al., 2004). Maraston et al. (2001) suggest that W3 has an age of $\sim 0.3 - 0.5$ Gyr and a metallicity of $\sim 0.5Z_\odot$, which place this GC in the exact age and metallicity ranges where we want to test the model presented in M05. Its high mass ($\sim 10^8 M_\odot$) is two orders of magnitude more massive than any other GCs (Maraston et al., 2004). For example, in the "Antennae", comparable GCs have masses up to $\sim 10^6 M_\odot$ (Zhang & Fall, 1999)) . It assures the presence of every stellar phases but makes its classification not straightforward.

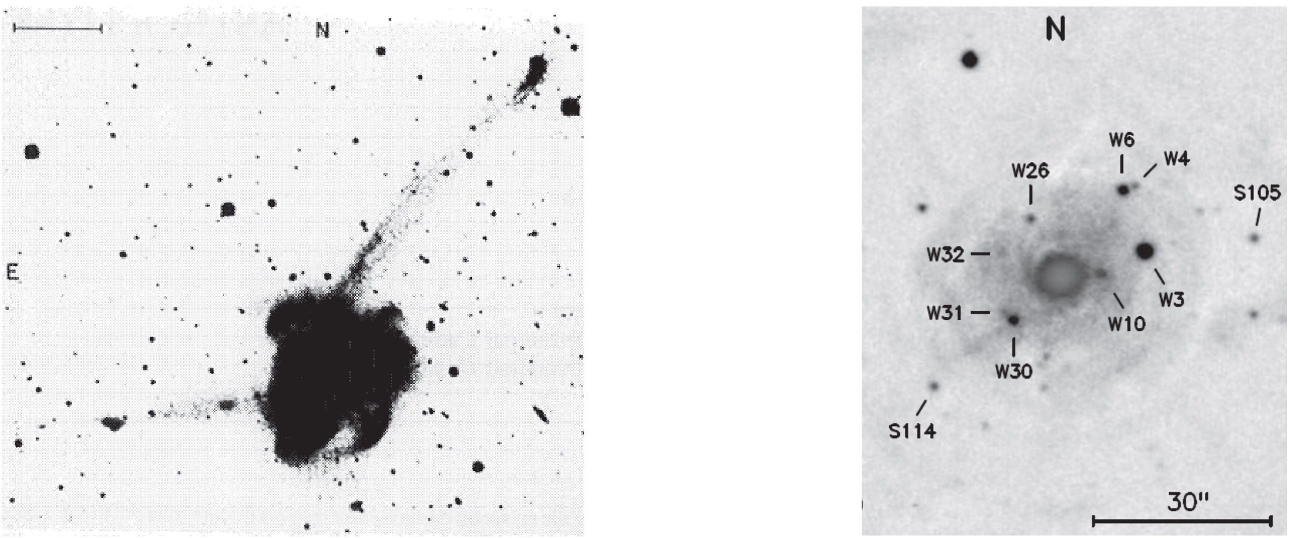

Figure 1.1.2: *Left panel* : Blue photograph of NGC 7252 from Schweizer (1982). The scale bar is 1'= 28kpc. *Right panel* : Blue-light image from Schweizer & Seitzer (1998) showing the main star clusters in the nearby NGC 7252.

We have chosen to study this object especially because of its high brightness, which make this target much easier to observe.

[2] $http://leda.univ-lyon1.fr//$ on July 2009
[3] See Appendix

1.2 Hertzsprung-Russel Diagram

1.2.1 Overview

The Hertzsprung-Russel (HR) diagram shows the relation between the luminosity and the temperature of stars[4]. For a given sample of stars coming from the same cloud of gas, most of them occupy the *Main Sequence* region (see Figure[5] (1.2.1)). Indeed, that stage, where stars are fusing Hydrogen into Helium in their cores, is the longest one. We can also distinguish 3 others main groups : Giants, Supergiants and White Dwarfs. These latter are the next stages coming after the main sequence when all the Hydrogen has been consumed. During its evolution, a star moves through the diagram, and follows a path depending on its mass. We can track this path for a given mass as indicated on Figure[6] (1.2.1).

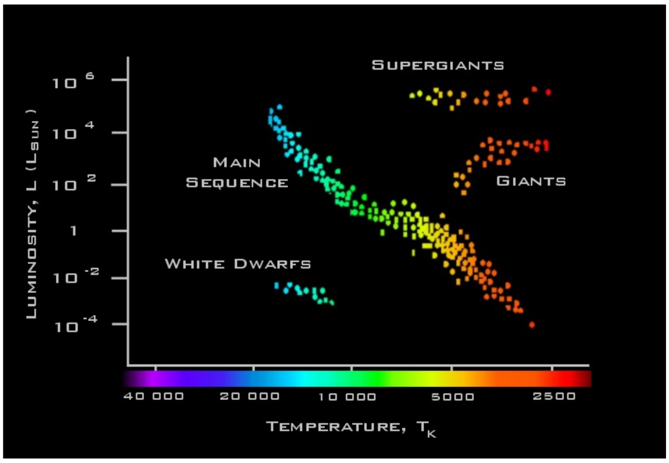

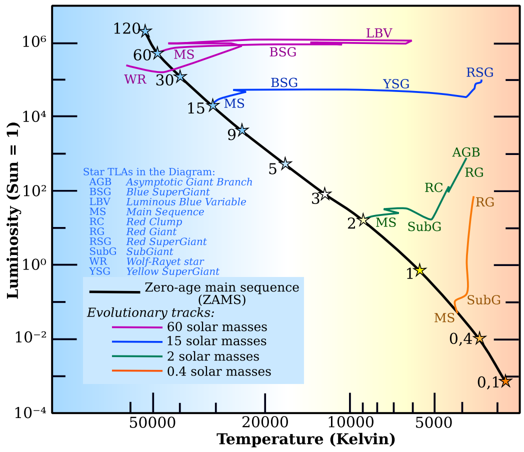

Figure 1.2.1: *Left panel* : a typical HR diagram . *Right panel* : stellar tracks are highlighted.

The metallicity of an object is the proportion of its matter made up of chemical elements other than hydrogen and helium. It may provide an indication of its age : when the Universe formed, it consisted almost entirely of hydrogen. Over time, nucleosynthesis in stars creates heavier elements increasing the metallicity. Therefore, older stars have lower metallicities than younger ones. From this conclusion, and assuming the hierarchical clustering, we can expect that massive galaxies show higher metallicity.

1.2.2 AGB and RGB stars contribution in the K-Band

Let's focus now on a particular star class : an intermediate-mass star ($0.5 - 10\ M_\odot$), will evolve into a Giant. We have then several paths depending again on the stellar mass : the Red Giant Branch (RGB) for mass between ~ 0.5 and $\sim 5\ M_\odot$ and the Asymptotic Giant Branch (AGB) for mass between ~ 5 and $\sim 10\ M_\odot$. Each class is caracterized by a specific internal structure. The RGB stars are the most common red giants whose shells are still fusing hydrogen into helium, while the core is inactive helium. An AGB star also appears as a red giant. Its interior structure is however characterized by a central and inert core of carbon and oxygen, a shell where helium is undergoing fusion to form carbon, another shell where hydrogen is undergoing fusion forming helium and a very large envelope of material of composition similar to normal stars. These two star-classes are the biggest contributors to the K-Band light as shown on the right panel in Figure (1.2.2).

One of the AGB subclasses are the Carbon-stars (C-star) due to their carbon-richness in their atmosphere. Thus, thanks to the presence of Oxygen, a lot of CO molecules form, increasing particularly the CO features lines strength. However, this phase still presents some difficulties in theoretical modelling. As the AGB stars comes from higher mass stars, they are about much brighter than the RGB stars. But, the heavier a star, the faster it evolves toward a further stage which is less luminous. So, for an intermediate-age (~ 1 *Gyr*) sample of stars, the AGB stars dominates the luminosity but, for an old (~ 10 *Gyr*) sample of stars, they are outnumbered[7] by the RGB stars which then become the dominating class.

[4] We can find others presentations such as Absolute Magnitude vs (B-V) colour index

[5] from www.le.ac.uk on june 2009

[6] from www.wikipedia.fr on june 2009

[7] for a 15 Gyr old sample : $\frac{N_{RGB}}{N_{AGB}} \sim 10^3$ from Renzini (1998)

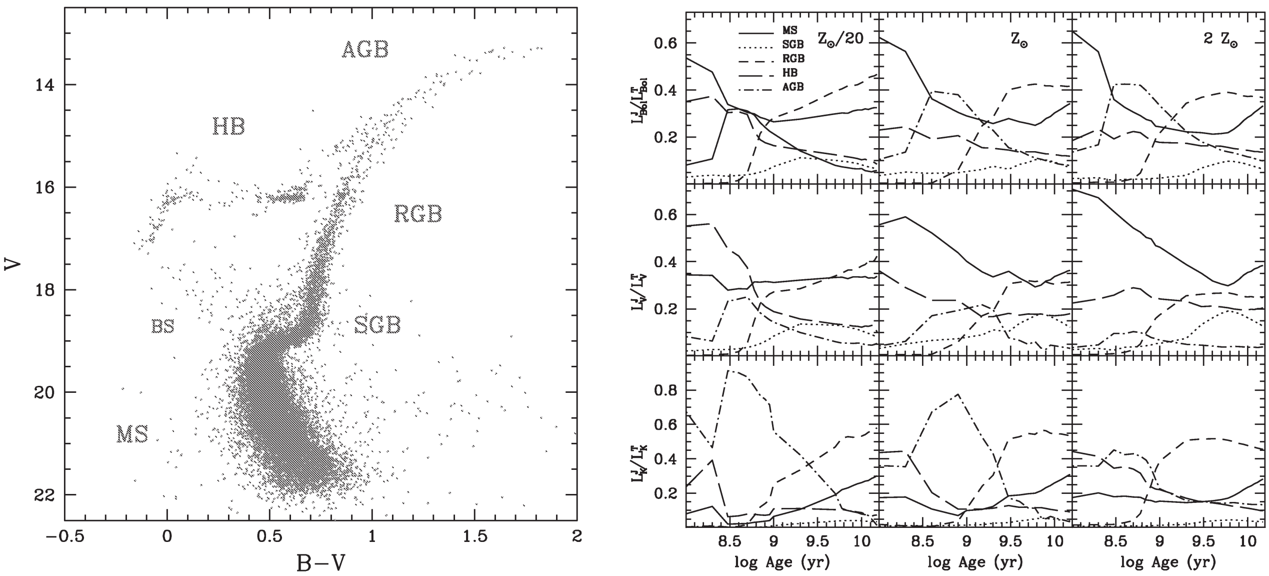

Figure 1.2.2: *Left panel* : HR diagram for an old star cluster. *Right panel* : Luminosity contributions in bolometric, V and K bands (from top to bottom) of evolutionary phases and their dependences on age and metallicity. From left to right, metal-poor, solar metallicity and solar-rich SSPs are shown. Note that the y-scale of the bottom panel is not the same as in the others two panels. Note also that 9 log age (yr) $\hat{=}$ 1 (Gyr), and 10 log age (yr) $\hat{=}$ 10 (Gyr).

1.3 Motivations of this project

1.3.1 Optical limits, a need for near-IR analysis

One of the main approaches for studying galaxy formation and evolution is to explore nearby early-type galaxies, by means of their present stellar populations. In the last decades this search was mainly performed in the optical wavelength window, due to the availability of the needed instrumentation. But even with the appearance of 8m-class telescopes and the Hubble Space Telescope, the majority of the galaxies, almost all outside of the Local Group, remain still unresolvable. Thus we have to rely only on their integrated light. Significant progress has been made with the development of the Evolutionary Population Synthesis models (EPS)(e.g. M05). This technique allows us to model the spectrophotometric properties of stellar populations, using the knowledge about the stellar evolution. The simplest approach to the EPS models is the Simple Stellar Population (SSP). With SSPs we describe populations of stars which share the same chemical composition and age, i.e. they came from the same initial molecular cloud. By matching the strength of carefully selected combinations of features in the observed object spectra to the output of the EPS codes, one can derives estimates of stellar population properties such as ages, metallicities, stellar mass functions, etc. But still many of the results remain uncertain, due to the fact that in the optical light (e.g. in the V-band) the contribution from several important stellar evolutionary stages is almost equal (see Figure (1.2.2)). In spite of significant efforts in the last decade toward resolving this issue (e.g. Worthey et al. (1994)), there is a need of new indicators, which react only to one parameter of the stellar population, with no or insignificant contribution from the others.

The near-IR wavelength range offers a new insight into the evolutionary paradigm. The K-band light of stellar populations with ages between 0.3 and 2 Gyr is dominated by one single component, AGB stars (see Figure (1.2.2)). For populations with age $\geqslant 3Gyr$, the near-IR light is dominated by the RGB stars whose contribution stays approximately constant over large time scales (M05). By isolating the spectrophotometric signature of these stellar evolutionary phases one can hope to gain a better understanding of the properties of the integrated stellar populations. In particular, Mármol-Queraltó et al. (2008) (hereafter MQ08) have shown that the deep absorption feature at $2.3\mu m$, caused by the CO molecule rotation in the stellar atmospheres, is dependant on the metallicity. However, the interpretation of these results clearly awaits the predictions of more sophisticated EPS models. Presently they still have the largest uncertainties in the near-IR, partly due to the lack of well calibrated spectral libraries.

1.3.2 Using GCs as model calibrator

The modern stellar population models are constructed by summing up the flux from stellar populations which populate a given isochrone. To build such models there is a need for large spectral libraries of stars, from which one determines how the Spectral Energy Distribution (SED) depends on parameters like stellar effective temperature, gravity and metallicity. Then this information is coupled with theoretical stellar evolutionary isochrones and stellar flux distribution to produce the SED of the model population. This method produces stellar population models, which are tuned to the specific chemistry and star formation history of the Milky Way, because it relies on the spectral properties of stars in our galaxy.

Such model is the one computed by M05. It evaluates the flux contributions of Post Main Sequence (PMS) stars. This method has several advantages, the most important of which is the inclusion of some important, but theoretically less well known stellar evolutionary phases, like the AGB phase. This phase is much more difficult to include in the spectral synthesis method, because the complete stellar tracks are not available, due to difficulties in theoretical modelling of mass-loss, dredge-up, and thermal pulses (e.g. Cassisi et al. (2001)). The AGB stars are particularly important for the study of stellar populations in the near-IR, where their contribution can reach up to 40% of the total K-band light (M05).

For the computation of theoretical stellar population SEDs, large and well calibrated stellar spectral libraries are needed, containing stars at different evolutionary stages and with different chemical composition. In order to calibrate or check the predictions of the models, we can observe GCs. Indeed, stars do not form in isolation, but in large complexes, and thus all of them share the same initial chemical composition and age. The GCs are the closest objects of the SSPs because their evolution is only controlled by their initial mass. In spite of some complications[8] (e.g. the existence of a double main sequence in the Galactic Globular Cluster ω Centauri by Anderson (1997) and Bedin et al. (2004)), GCs still remain the best available empirical approximation for a SSP.

1.3.3 The model and this project

M05 developed a tool to predict the age and the metallicity from some near-IR indices, but, relying only on stars in -our galaxy-. Building the model, M05 have used a library of stars calibrated with few C-stars. They have derived their spectrophotometric properties and have deduced a high CO composition increasing a lot the D_{CO} index for intermediate-age population. Outside the Milky Way, L09b showed marked disagreement between its predictions and the observations for intermediate-age and half solar metallicity GCs. Moreover, L09a have studied others C-stars in the Large Magellanic Cloud (LMC) and have found less contribution to the D_{CO} index than expected by M05. This may come from different reasons : first, because of the different metallicity in the studied C-stars ; second, because of the C-stars pulsations.

This is the reason why we study the W3 cluster which is very massive. One can hope that this globular cluster can lodge enough C-stars to have every pulsation stages. We can have therefore an average value of the contribution of C-stars and then have a more reliable value for CO index. Moreover, every model has been calibrated on GCs inside the Local Group. For the first time, we study here an outside GC -and- in another age range, permitting us to reliably test the model.

For the same purpose, we study here the NGC 7252 early-type galaxy to test the model on another age range, outside the Local Group. Moreover, studying stellar populations through near-IR analysis of such merger may help in understanding galaxy fomation and evolution as explained in Section (1.1.1). However, the merging make the analysis more difficult to interpret since it summons by definition -not- a SSP.

[8]Throughout this report, we will not discuss such difficulties.

Chapter 2

Observations and Data Reduction

2.1 Observations

The W3 observations were carried out as part of Program 383.B-0625 (PI: Kuntschner) in service mode. At the time of the writing of this report only the K-band data was available and hence the analysis is limited to this data-set. Four Observing Blocks (hereafter OB) were carried out each with 9 times 300s on source integration. The standard ESO data-reduction pipeline was used by H. Kuntschner to provide calibrated and extracted spectra of W3. However, only two OBs produced useful data and therefore the individual spectra of those were combined into a single 1-dimensional spectrum of W3.

The observations for NGC7252 itself were carried out as part of the science verification for SINFONI. The public dataset was reduced with the standard ESO pipeline by M. Lyubenova and provided to O. Do Cao. One fully calibrated data cube is available for each spatial scale. In this report, we will often refer to NGC 7252 [100] and NGC 7252 [250]. The square bracketted numbers is only an abbreviation which indicates the spatial scale in milliarcseconds (mas) of the image. As the detector has 32x32 pixels, the image cover a Field of View (FoV) of 3.2 and 8 arcsec respectively. We observe therefore the very center of the galaxy.

2.2 SINFONI Integral Field Spectrograph

2.2.1 Instrument Description

Behind the abbreviation SINFONI stands the name of the Spectrograph for INtegral Field Observations in the Near Infrared, which is mounted on the Cassegrain focus of Unit Telescope 4 (Yepun) on VLT at Paranal La Silla Observatory. It covers the near-IR spectral domain ($1 - 2.5\ \mu m$) including the J, H and K-bands (see Table (2.1)). This instrument allows us to simultaneously obtain spectroscopy over a continuous field of view, which leads to a spectrum for each spatial pixel (or spaxel, as often called in the IFU[1] community). Later from these spectra one can reconstruct an image of the object under study.

Table 2.1: Some photometric near-IR bands, where λ_0 is the effective or central wavelength and $\Delta\lambda$ the full width at half maximum, assuming the filters have a gaussian transmission.

Name Spectrum	Effective wavelength (λ_0)	Bandpass($\Delta\lambda$)
J	1.25 μm	0.12 μm
H	1.66 μm	0.16 μm
K	2.22 μm	0.22 μm

2.2.2 Datacube

The output data format of SINFONI records both spatial and spectral dimensions. For each spaxel the spectrum is recorded, therefore giving the third dimension to the data. This is then referred to as 3D spectroscopy.

[1] Integral Field Unit

The X and Y axis of the data cube store the spatial information, right ascension and declination, or the image of the object under study. Along the third axis we have a spectrum for each spatial pixel.

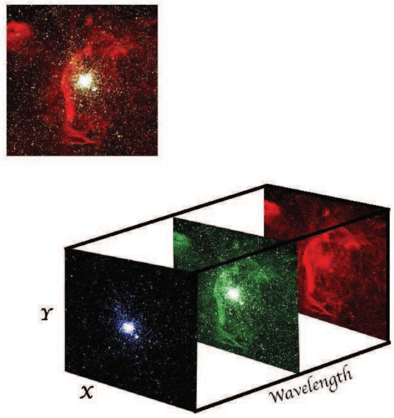

Figure 2.2.1: Principle of the data cube. The X and Y axis keep the spatial information, while along the Z direction a spectrum for each spaxel is stored. This cartoon shows how NGC1850 looks in different wavelength planes of the data cube. While the blue band contains light only from the young, hot stars, in the narrow filter $H\alpha$ the glow of the surrounding gas is also visible. (NGC1850 image credits – ESO.)

The advantage of the data cube is that a variety of data analysis techniques are applicable. By collapsing the cube in the Z direction, we obtain a reconstructed image of the science object. Then we can treat this image with the ordinary broad band photometry techniques. Furthermore, each slice of the data cube along the spectral direction is a monochromatic image of the object. Thus we can easily extract one or several narrow band images, centred around some specific spectral features. This principle is shown on Figure (2.2.1), where a colour composite image of the young star cluster in the Large Magellanic Cloud NGC1850 (top) is dispersed and stored in a schematic data cube (bottom). As an example, three filters have been simulated – the broad bands B (blue) and V (green) and the narrow band $H\alpha$(red). For each spatial pixel there is and associated spectrum, which contains kinematical and chemical composition information about the science target. By exploring these spectra, we can reconstruct the velocity profile of the object, as well as its stellar population properties. After comparison with stellar population models we can directly look at the age or metallicity distribution.

2.3 Near-Infrared K-Band

2.3.1 Definition of indices (Lick System)

One of the most successful diagnostic tool which has been developed to measure spectral indices, was the Lick/IDS system in the optical wavelength range (e.g Faber et al. (1985); Worthey et al. (1994); Trager et al. (1998)). It consists of 21 spectral indices originally, covering the strongest features in the optical, and has been extended later.

The line strengths in this system are measured like equivalent widths. The definition of each index consists of a central passband on the feature, which is flanked to the blue (b) and to the red (r) by pseudo-continuum passbands. First the average flux in the pseudo-continuum passbands $< F_r >$ and $< F_b >$ is computed following equation (2.3.1) and (2.3.2).

$$< F_r > \quad = \quad \frac{1}{r_2 - r_1} \int_{r_1}^{r_2} F(\lambda)\, d\lambda \tag{2.3.1}$$

$$< F_b > \quad = \quad \frac{1}{b_2 - b_1} \int_{b_1}^{b_2} F(\lambda)\, d\lambda \tag{2.3.2}$$

where r_1 and r_2 (respectively b_1 and b_2) are the red (respectively blue) wavelength boundaries, and $F(\lambda)$ the flux at the wavelength λ.

The local continuum is determined after drawing a straight line between the midpoints of the blue and the red continuum levels. The index EW (where Equivalent Width is defined such as EW is positive for an absorption line) is then the difference in flux between the central passband $F(\lambda)$ and this continuum level $F^{cont}(\lambda)$, given by equation (2.3.3).

$$EW = \int_{c_1}^{c_2} \frac{F^{cont}(\lambda) - F(\lambda)}{F^{cont}(\lambda)} \, d\lambda \tag{2.3.3}$$

where c_1 and c_2 are the central passband boundaries.

2.3.2 Near-IR index measurement procedure

The principle of computing the value of a near-IR index is the same as in the optical Lick system. Figure (2.3.1) shows as an example the NaI index. The central passband, marked with vertical solid lines, is surrounded by a blue and a red pseudo-continuum passband (the vertical dashed lines). The wavelength boundaries we have used are given in table (2.2).

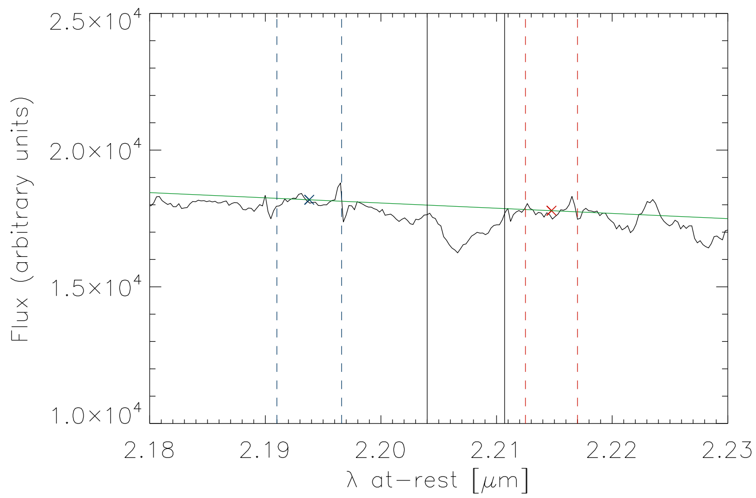

Figure 2.3.1: Outline of the index measurement procedure. A spectrum of NGC 7252 [100] is shown. The vertical solid lines mark the extent of the central passband NaI. The vertical dashed lines show the blue and red pseudo-continuum passbands. During the measurement procedure the level of the flux in the blue and red passbands is determined, marked here with blue and red crosses, respectively, and a straight line between these two values is drawn to define the local continuum level.

The average fluxes in the two pseudo-continuum bands are computed following Equation (2.3.1) and (2.3.2) and are marked on figure (2.3.1) with a blue and a red cross, respectively. The local continuum level is defined by drawing a straight line between the centres of the pseudo-continuum bands at the levels of the average fluxes. Then Equation (2.3.3) is applied to get the index value. The indices from the table into the figure (2.3.2) are all computed in this way except the CO features which are discussed in section (2.3.3). Before measuring the index, the spectra were brought to zero rest-frame velocity.

2.3.3 The $^{12}CO(2-0)$ molecular index

The indices, which measure the strength of the $^{12}CO(2-0)$ band-head, have slightly different definitions, as compared to atomic indices. Figure[2] (2.3.2) shows the unusual and asymmetric shape of this very broad feature. For this reason, MQ08 defined (as in the Lick system) a local continuum level, but with two blueward pseudo-continuum passbands instead of one blue and one red (see Figure (2.3.3)). MQ08 proposed to measure the CO at $2.29\mu m$ as a *generic discontinuity*, i.e. as the ratio between the average fluxes in the continuum $< F_{continuum} >$ and in the absorption band $< F_{abs} >$ (see Equation (2.3.4) using previous notations). The wavelength intervals of this index is listed in Table (2.2).

[2]From L09b

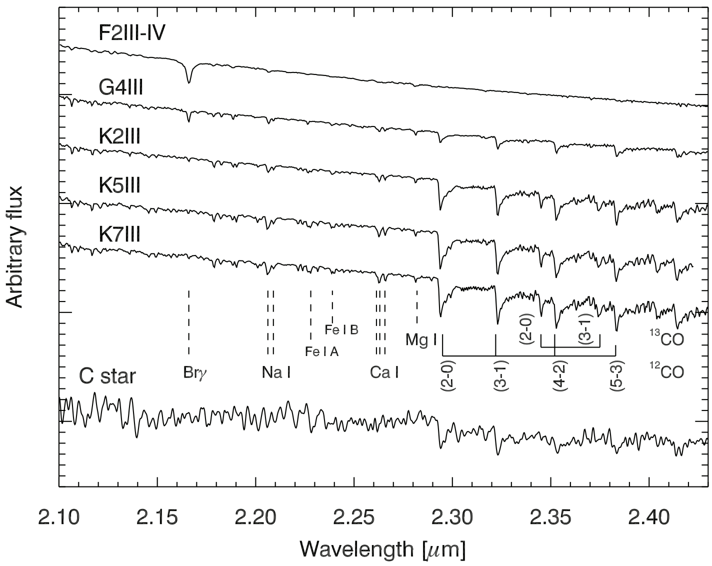

Species	$\lambda[\mu m]$
Br_γ	2.1661
Na I	2.2062
Na I	2.2090
Fe I A	2.2263
Fe I B	2.2387
Ca I	2.2614
Ca I	2.2631
Ca I	2.2657
Mg I	2.2814
^{12}CO(2-0)	2.2935
^{12}CO(3-1)	2.3226
^{13}CO(2-0)	2.3448
^{12}CO(4-2)	2.3525
^{13}CO(3-1)	2.3739
^{12}CO(5-3)	2.3829

Figure 2.3.2: *Left panel* : spectra of giant stars from different spectral types, taken from the SpeXIRTF Spectral Library (Rayner et al. (2007)). The location of several spectral features is indicated. The spectrum at the bottom of the plot is of a carbon star in the LMC cluster NGC2162, observed with SINFONI and smoothed to the spectral resolution of the SpeX Library. The increased amount of features, as compared to the other spectra, is not due to low S/N, but these are real absorption lines, due to CH, CN, etc. *Right panel* : the main spectral features in the K-Band.

$$
\begin{aligned}
< F_{continuum} > &= \frac{\int_{r_1}^{r_2} F(\lambda)\, d\lambda + \int_{b_1}^{b_2} F(\lambda)\, d\lambda}{(r_2 - r_1) + (b_2 - b_1)} \\
< F_{abs} > &= \frac{\int_{c_1}^{c_2} F(\lambda)\, d\lambda}{c_2 - c_1} \\
D_{CO} &\equiv \frac{< F_{continuum} >}{< F_{abs} >} \qquad (2.3.4)
\end{aligned}
$$

Table 2.2: D_{CO} definition from MQ08 and NaI definition from Frogel et al. (2001)

Index name	Continuum Bands $[\mu m]$	Feature passband $[\mu m]$
D_{CO}	2.2460 - 2.2550	2.2880 - 2.3010
	2.2710 - 2.2770	
NaI	2.1910 - 2.1966	2.2040 - 2.2107
	2.2125 - 2.2170	

To confirm the results from the recent D_{CO} definition, we will also use the CO index defined by M05, which measures the ratio of the flux densities at 2.22 and $2.37\mu m$, based on the HST/NICMOS filters F222M and F237M (see Figure (2.3.3)). The index is computed in units of magnitudes and is normalised to Vega. This index reflects the strength not only of $^{12}CO(2-0)$, but also of the other CO absorption features redwards from $2.3\mu m$. However, some spaxels show artefacts (see an example in Figure (2.3.4)) in the filter F237M due to dead pixels or unsufficient data reduction, so we excluded[3] them during the measurement of the intrinsic value. Moreover, the extremities of the detector must be systematically left aside for the analysis because of the unrelevant counts above $\sim 2.39\mu m$. In order to counter this effect for measuring the CO index properly, we have extrapolated the continuum by a linear fit to this region.

[3] For example, for n7252 we have excluded 47 defectuous bins out of a total of 365 bins

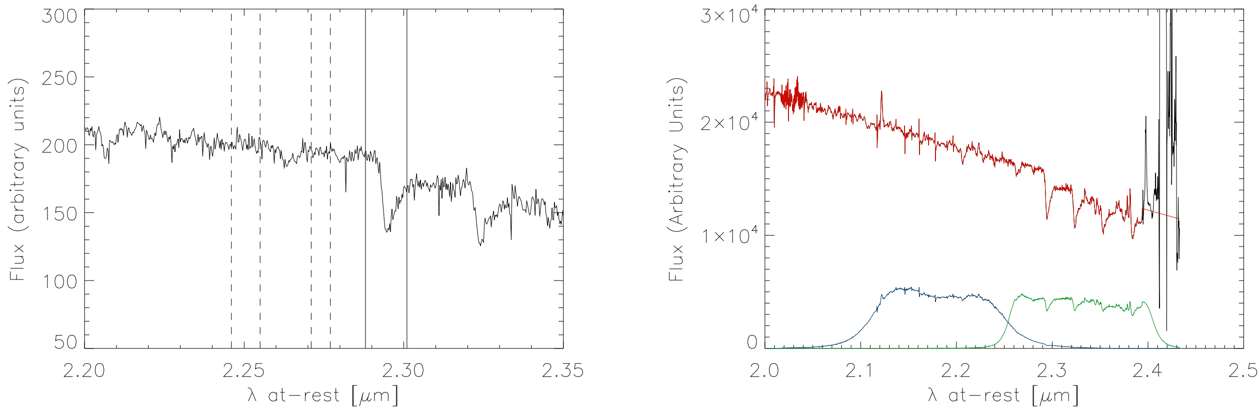

Figure 2.3.3: *Left panel* : wavelength ranges of the generic discontinuity D_{CO}, defined by MQ08. The pseudo-continuum passbands are marked with dashed lines, while the feature passband is surrounded by solid lines. *Right panel* : wavelength ranges of the CO index defined by M05. The HST filters F222M and F237M multiplied by the red spectrum is shown in blue and green respectively. The corrected (red) spectrum is exactly the same as the observed (black) one but where we have extrapolated the spectrum by a straight line above $\sim 2.39 \mu m$, because of artefacts due to the instruments.

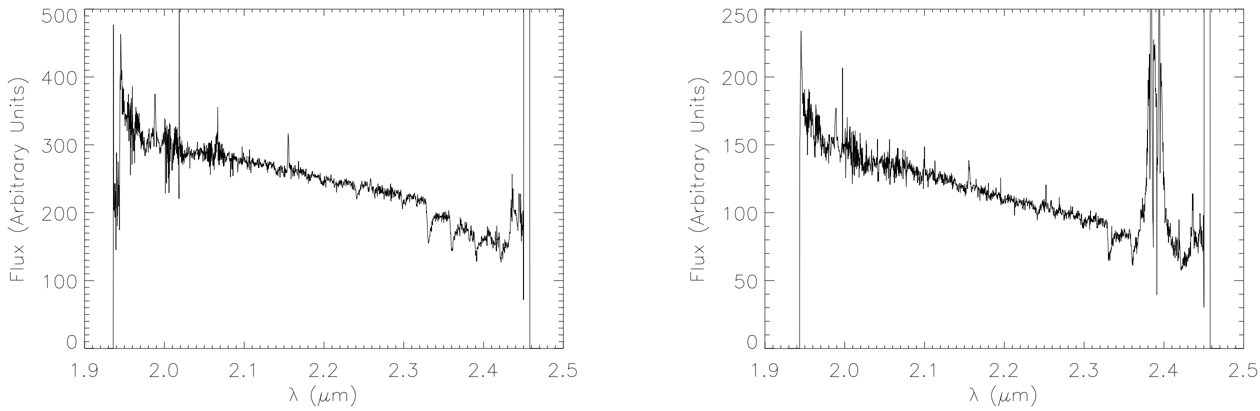

Figure 2.3.4: Comparison between a normal spectrum (*left panel*) and one affected by an artefact at $\sim 2.39 \mu m$ (*rightpanel*).

2.4 Data Reduction

2.4.1 Sky in near-IR and Telluric Corrections

The data reduction has been performed by Harald Kuntschner. He provides the reduced datacube and the associated noise spectrum (see Figure (2.4.1)) to make error estimations. Then from these data, I have made the following steps.

One of the main contributors to the detector counts, when observing an astronomical target in the near-IR, is the very bright night sky which often may produce more counts than the scientific target itself. Below 2.2 μm the sky emission is dominated by OH emission lines. Red-wards from this wavelength, the thermal background from the atmosphere and the telescope dominates. In order to correct for this contributions, the usual observational technique is to point the telescope consecutively to the target and an empty region on the sky, i.e. to nod the telescope, and afterwards subtract the latter from the former. This is the so called OS technique (O stands for object, S - for sky).

Another imprint on the near-IR science spectra, originating in the Earth's atmosphere, are the telluric absorption lines. These are the most prominent features in the near-IR and are especially deep in the blue end of the K-band. Thus we have to observe telluric calibration stars as close as possible in time and space to the science target observation and with the same instrument setup. Then we have to remove them from the spectrum.

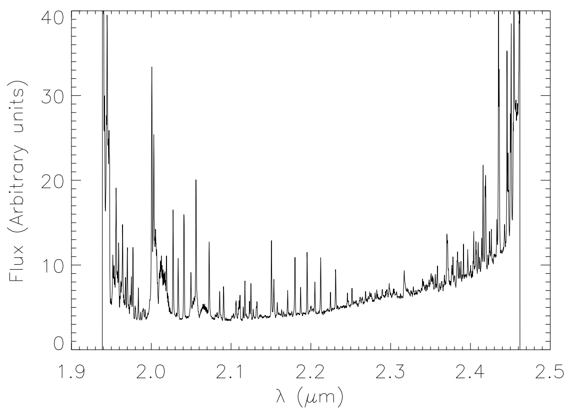

Figure 2.4.1: Noise spectrum in the K-Band. Below $\sim 2.2\ \mu m$, light is dominated by sky emission ; above $\sim 2.3\ \mu m$, by the thermal background from the atmosphere and the telescop itself.

When the goal of the observations is to obtain precise photometry or to measure accurately line strengths, it is very important to achieve as good as possible removal of the signature of the night sky. For example if one underestimates the sky background, this will lead to a decrease of the line strength of a given absorption feature. Underestimating the sky by only 4% will lead to a decrease of 1Å for the NaI feature at $\sim 2.2\mu m$ which has a typical strength of 3 - 5Å for Fornax cluster galaxies (Silva et al., 2008). Another source of error is the inaccurate telluric correction which may introduce new features in the science spectra.

In this study, we have reached a S/N of 47, 177 and 235 for W3, NGC 7252 [100] and NGC 7252 [250] respectively to measure the R_8 values[4].

2.4.2 Voronoi 2D-Binning

In order to extract stellar kinematics from Integral Field Spectroscopy, binning is recquired for proper analysis. Figure (2.4.2) shows the difference between spectra with high and low Signal-to-Noise ratio (S/N). In the latter case, features are almost completely drowned into stochastic fluctuations.

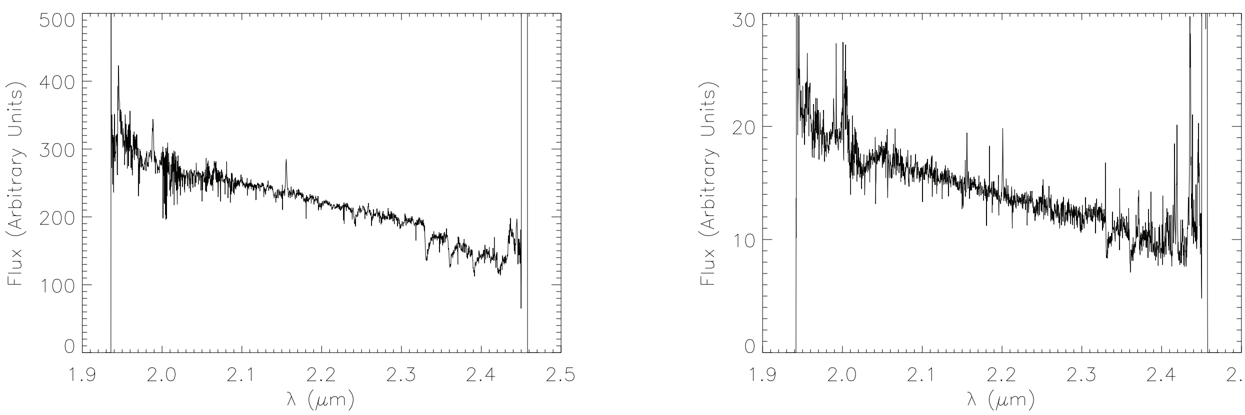

Figure 2.4.2: *Left panel* : a spectrum extracted from the center of NGC 7252. *Right panel* : a spectrum from the periphery of the same galaxy. Note that the flux is in arbitrary units but has the same scale for both of the spectra, such as the center has a S/N of about ten times higher than the periphery. The very extrem counts above $\sim 2.45\mu m$ and below $\sim 1.95\mu m$ are artefacts. However, the peak at $\sim 2.0\mu m$ is due to the sky emission as shown in Figure (2.4.1)

[4]Defined in Section (3)

It's therefore crucial to bin several spaxels to enhance the S/N and get reliable measurements. The Voronoi 2D-Binning Method from Cappellari & Copin (2003) (hereafter V-Binning) provides a software which permits to reach a chosen constant $(SN)^{target}$ per bin, but loosing spatial information. The output data is a binned map where we have a visual information on how the light is distributed. In each bin, we have finally one single spectrum whose Signal-to-Noise ratio is roughly $(SN)^{target}$ (see figure (2.4.3)).

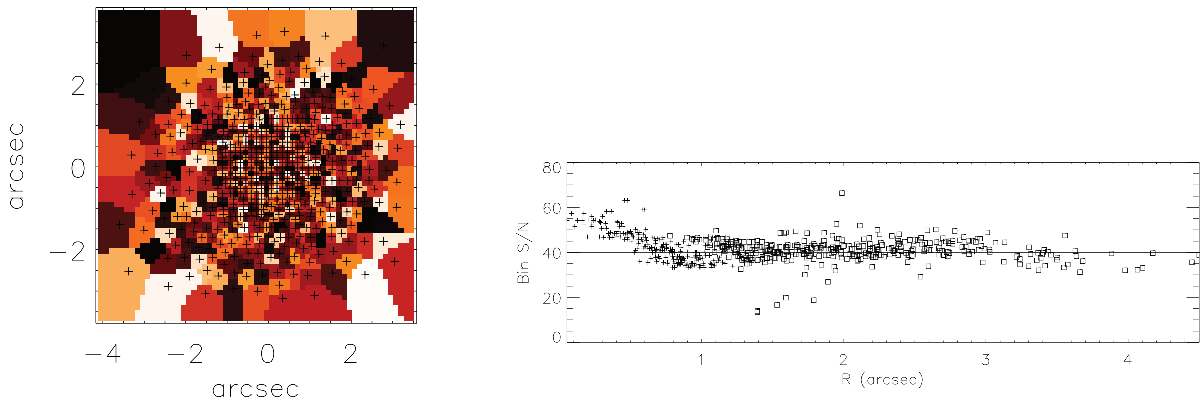

Figure 2.4.3: Outputs of V-binning. *Left panel* : binned map of reached S/N : bigger the bin is, the lower is the initial signal. Black crosses give the bin spatial coordinates. *Right panel* : the horizontal line shows the target S/N while empty square indicates real reached value. Leaving aside some irrelevant points around $R \sim 1-2$ *arcsec*, we can see that the farthest bins (beyond ~ 3 *arcsec*) don't reach the target value (here 40) due to very low initial signal.

We have to choose an appropriate $(SN)^{target}$ to be able to measure kinematic values with enough accuracy but without loosing too much spatial information. For this study, $(SN)^{target} = 40$ is a good compromise : the resulting error for v and σ is ~ 3 $km.s^{-1}$, we have an error of about 0.1% and 1% respectively compare to the absolute range.

2.4.3 Penalized Pixel Fitting (pPXF)

Each reducted bin is affected by a different recession velocity due to a possible rotation of the astronomical target. In order to perform proper measurement of indices, we have to de-redshift each binned spectrum. Cappellari & Emsellem (2004) provides a software able to measure the velocity v and the velocity dispersion σ from a given redshifted spectrum and a sample of star SEDs at rest. By comparing linear combinations of the latter to the input spectrum, pPXF gives the best match of v and σ. In our case, few types of K and M giant stars (~ 10) seem to fit correctly the observed spectra.

pPXF is able to *clean* the input spectrum by not taken into account some datapoints too far away from the fit. Basically, this option is activated when the difference between the observed spectrum and the fit is greater than 3σ error. In this report, we have used the *clean* option, expecting to get more reliable values by getting rid of irrelevant datapoints. This operation is shown on the spectrum by green straight lines, and in blue when a continuous part of the spectrum has been left aside (see Figure (2.4.4)).

As we can see in table (2.4.4), the *clean* option has only a very tiny effect on the values calculated through the pPXF process : values changed by less than 0.01%. Indeed, the D_{CO} index strength is the most constrainting feature and is not affected so far.

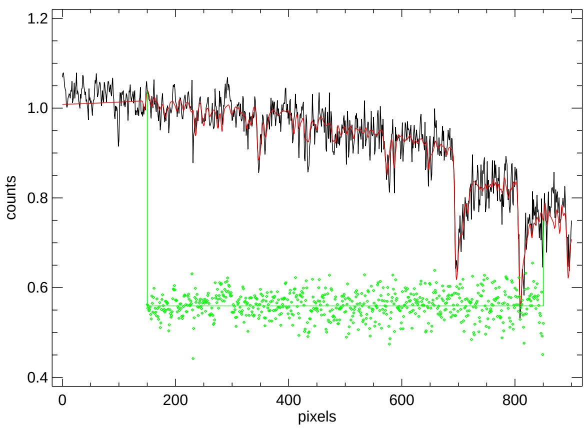

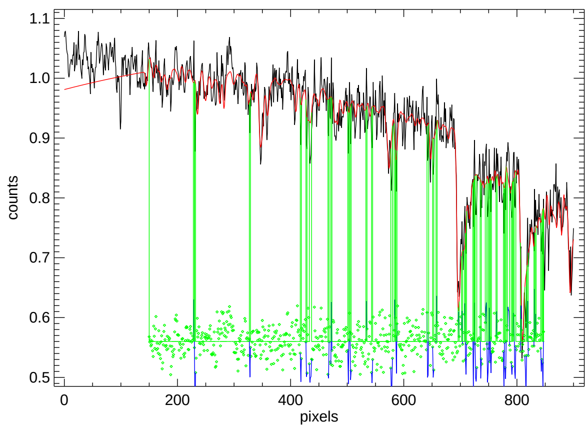

Name	$v[km.s^{-1}]$	$\sigma[km.s^{-1}]$
NGC 7252 (100)	4757.2 ± 2.3	112.2 ± 3.4
NGC 7252 (250)	4751.8 ± 1.7	110.3 ± 2.6
W3	4776.7 ± 5.2	41.6 ± 8.0

Name	$v[km.s^{-1}]$	$\sigma[km.s^{-1}]$
NGC 7252 (100)	4757.2 ± 2.3	112.2 ± 3.4
NGC 7252 (250)	4751.8 ± 1.7	110.3 ± 2.6
W3	4776.7 ± 5.2	41.6 ± 8.0

Figure 2.4.4: The two spectra are pPXF output for NGC 7252. The results in the right column has been derived with the *clean* option on the contrary to the left column. The red spectrum is the fit produced by pPXF of the black (observed) spectrum. Green dots represents the difference between the fit and the observed spectrum. Green straight lines (respectively blue lines) shows where datapoints (respectively whole part of the observed spectrum) has been neglicted during the operation.

Chapter 3

Results

In order to measure reliably kinematics and line strengths, we have to spatially bin the datacube to a roughly constant S/N ratio. This was done using V-Binning and choosing $S/N^{target} = 40$ (see Section (2.4.2)). The extraction of the kinematical information was performed with the help of the pPXF with *clean* option (see Section (2.4.3)). In order to calculate one single value from a map for a given quantity, Kuntschner (2000) defined a pratical[1] radius $R_8 = R_{eff}/8$ (with $R_{eff} = 14.6\ arcsec$)[2], where R_{eff} is the effective[3] radius. By summing all the bins whose distance to the center is less than R_8, we obtain a new summed spectrum from which we can derive a single value for the kinematics and indices (hereafter R_8 values). For W3, we relied on a fully integrated spectrum provided by H. Kuntschner. The first section presents the results for both of the reduced datacube NGC 7252 [100] and NGC 7252 [250], while the second one presents those for W3. Then, the third part checks the results by plotting them with others early-type galaxies. Finally, the last section compare our results with the model from M05.

3.1 NGC 7252

3.1.1 Kinematical maps

In Figure (3.1.1), we present the two FoV for NGC 7252. The velocity v shown on the map are the difference between the real value and the recession velocity of the object defined as the median value of every measured velocities. The difference has been defined such as a positive value means moving redward.

We can clearly see the rotation of the galaxy and the high mass density in the center derived[4] from the peak on the velocity dispersion map. Note that grey bins in the galaxy outskirts are unphysical values due to too low achieved S/N.

On Figure (3.1.2), we compare all the measured kinematics values. We have then binned the values within 0.1" to have a better comparison[5]. Both of v and σ show an excellent agreement between the two FoV. On the velocity dispersion map [100], we have evidence for structure on a quarter of ring where σ is higher. However, this observation is not confirmed by the [250] FoV and needs further analysis. The rotation curve is a little bit steeper on [100] but can be explained by the difference of spatial scale. The R_8 values for both of the datacubes are listed in Table (3.1).

3.1.2 D_{CO} Index map

Then, we mesure the D_{CO} index in each bin. However, we have not build such map for the CO index due to the too large number of artefacts (see Section (2.3.3)). Because of the weakness of the NaI line strength (about 50 times weaker), this index map is neither available.

First, we can notice that the D_{CO} index shows the same symmetry as the luminosity indicated by countours in Figure (3.1.2). We can also clearly see the line strengh gradient, which is stronger in the center and become

[1]Definition for observation instead of the effective radius which is too large to be observed.
[2]from *http://nedwww.ipac.caltech.edu* on July 2009
[3]Radius within which half the total luminosity is emitted
[4]See Appendix.
[5]Error bars are computed by the standard definition : ratio between standard deviation of the dataset and squareroot of number of points-1

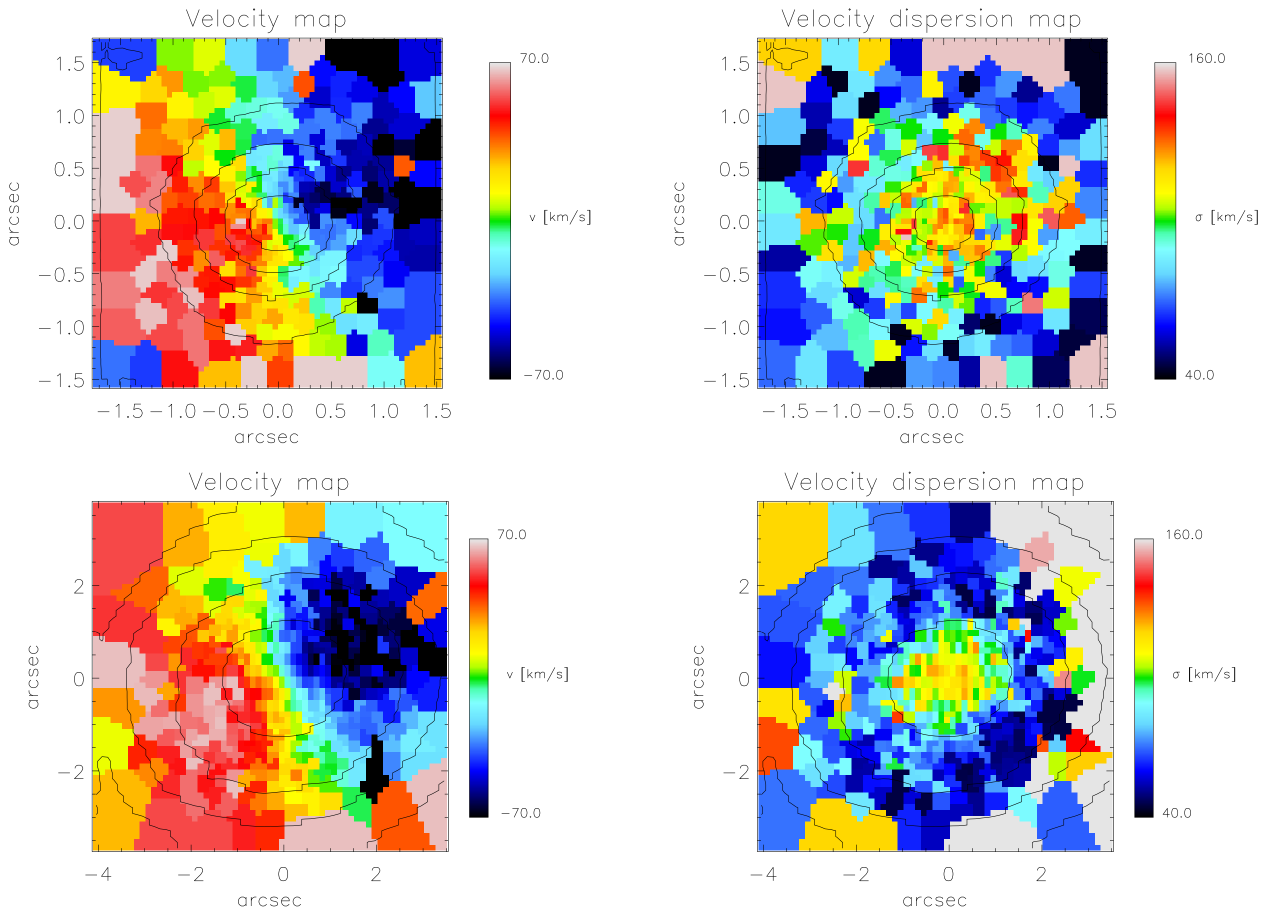

Figure 3.1.1: Solid lines are isophots to highlight galaxy symmetry. Note that the color scale are the same for both of the FoV. *Top panels* : kinematical maps for NGC 7252 [100]. *Bottom panels* : those for NGC 7252 [250].

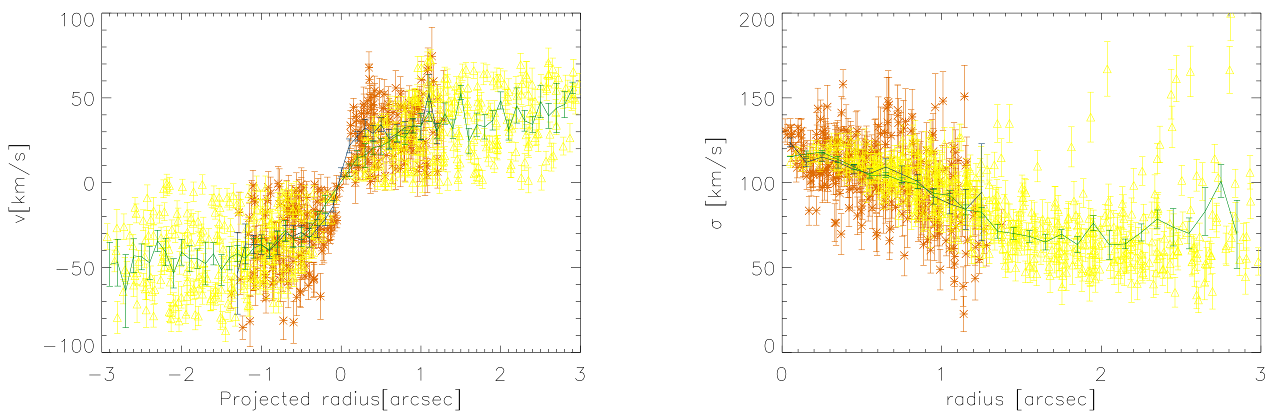

Figure 3.1.2: Comparison of the kinematical results between the two fields of view. The yellow (respectively orange) datapoints represents the [250] (respectively [100]) FoV. The green (respectively blue) solid line represents the mean value in 0.1" bin of the [250] (respectively [100]) FoV. We have decided to exclude in the plot bins containing more than 15 spaxels. In grey are bins with no available data due to too low S/N. The solid lines are isophots to highlight galaxy symmetry. *Left panel* : Velocity v comparison. *Right panel* : Velocity dispersion σ comparison.

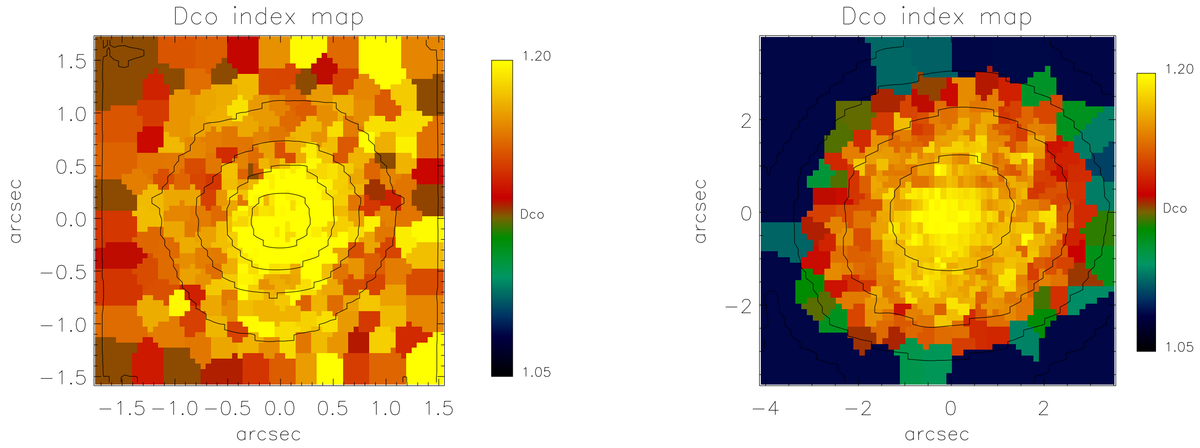

Figure 3.1.3: Comparison between the two FoV for the D_{CO} index. As previously, solid lines are isophots to highlight galaxy symmetry. Note that the color scale are the same for both of the FoV. *Left panel* : D_{CO} map for NGC 7252 [100]. *Right panel* : D_{CO} map for NGC 7252 [250].

weaker on the periphery. This metallicity gradient is characteristic of early-type galaxies.

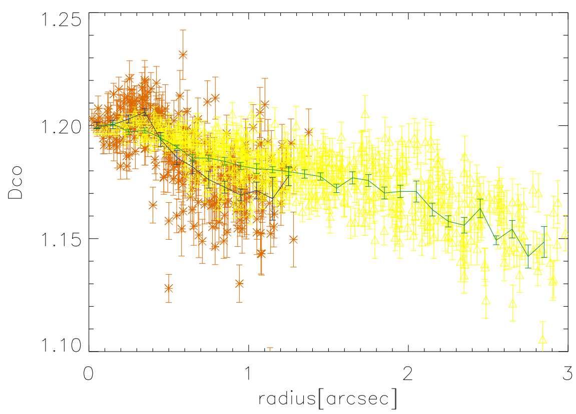

Figure 3.1.4: D_{CO} comparison. The color code is the same as the one used in Figure (3.1.2).

At the first order, the D_{CO} values agree with each other. However, the [100] FoV may show an internal structure not confirmed by the other one. Such structure can be studied but is beyond this project. R_8 D_{CO} value is given in Table (3.1).

Let's compare now the R_8 values between NGC 7252 [100] and [250]. We should find the same values for every measurement in common between the two FoV. While the results are the same for v, σ and D_{CO} within the error bars, the CO and NaI index show marked disagreement. However such differences may be explained by the difficulties in measuring CO and NaI. The error bars might be also underestimated due to their unusual estimation (see Section (2.4)), especially with the CO index where we have made an extrapolation beyond $\sim 2.39\mu m$ by hand. The values can change dramatically ($\sim 30\%$) according to the manner of defining the extrapolation. However the results remains in the same order compare to the absolute range of the indices[6], we will therefore consider these results as only qualitative.

[6]e.g. $-0.1 \leq CO \leq 0.3$ and $2 \leq NaI \leq 6$

3.2 W3

With one single summed up spectrum, we were able to calculate only the R_8 values for v, σ, D_{CO}, CO and NaI. All the results are listed in Table (3.1).

Table 3.1: Main results. The ages are taken from Maraston et al. (2004)

Name	v $[km.s^{-1}]$	σ $[km.s^{-1}]$	D_{CO}	CO [Å]	NaI [mag]	Age [Gyr]
NGC 7252 [100]	4757.2 ± 2.3	112.2 ± 3.4	1.194 ± 0.002	0.074 ± 0.001	3.73 ± 0.10	1 ± 0.5
NGC 7252 [250]	4751.8 ± 1.7	110.3 ± 2.6	1.191 ± 0.001	0.040 ± 0.001	3.33 ± 0.07	1 ± 0.5
NGC 7252 [MEAN]	4754.5 ± 2.7	111.3 ± 1.0	1.193 ± 0.002	0.057 ± 0.002	3.53 ± 0.20	1 ± 0.5
W3	4776.7 ± 5.2	41.6 ± 8.0	1.182 ± 0.007	0.082 ± 0.002	3.25 ± 0.34	0.4 ± 0.1

W3 has an astonishing velocity dispersion, almost ten times higher than others GCs (e.g. Larsen et al. (2004)). With Equation (5.3.2), we expect then a mass of about a hundred times higher, consistent with previous measurements given in Introduction.

For the next analysis, we will always use the NGC 7252 [MEAN] values whose errors has been simply computed by half the difference between [100] and [250].

3.3 Comparison with others early-type galaxies

We can now verify the coherence of our results by comparing them with the data available from Mármol-Queraltó (2009) listed in Table (3.2). Half of these galaxies belongs to the Fornax galaxy cluster, and the others are in a low density environment. Galaxy evolution seems to be dependent of their neighbourhood. Figure (3.3.1) compares our results with the data from this Table.

Table 3.2: Near-IR indices for others early-type galaxies from Mármol-Queraltó (2009).

Name	σ $[km.s^{-1}]$	D_{CO}	NaI [Å]	$H\beta$ [Å]	Environment
NGC 3605	59.1 ± 7.0	1.203 ± 0.002	3.46 ± 0.08	2.03 ± 0.10	Low Density
NGC 3818	199.5 ± 20.7	1.212 ± 0.003	4.75 ± 0.12	1.52 ± 0.05	Low Density
NGC 4261	300.9 ± 29.4	1.211 ± 0.002	5.10 ± 0.26	1.63 ± 0.05	Low Density
NGC 4564	184.3 ± 24.8	1.231 ± 0.002	5.68 ± 0.14	1.60 ± 0.05	Low Density
NGC 4636	221.2 ± 23.7	1.214 ± 0.002	4.03 ± 0.14	1.53 ± 0.09	Low Density
NGC 4742	89.2 ± 9.6	1.225 ± 0.001	4.16 ± 0.03	3.30 ± 0.11	Low Density
NGC 5796	305.4 ± 22.3	1.221 ± 0.002	5.48 ± 0.21	1.50 ± 0.07	Low Density
NGC 5813	226.7 ± 25.7	1.210 ± 0.002	4.01 ± 0.14	1.59 ± 0.05	Low Density
NGC 5831	151.0 ± 14.5	1.222 ± 0.002	4.95 ± 0.08	1.99 ± 0.15	Low Density
ESO 382-G16	249.2 ± 21.0	1.212 ± 0.002	4.61 ± 0.14	1.42 ± 0.11	Low Density
ESO 446-G49	118.2 ± 12.6	1.219 ± 0.003	4.00 ± 0.11	1.78 ± 0.12	Low Density
ESO 503-G12	150.1 ± 17.9	1.221 ± 0.002	3.87 ± 0.08	1.86 ± 0.10	Low Density
NGC 1316	226.0 ± 8.0	1.226 ± 0.002	4.61 ± 0.15	2.39 ± 0.11	Fornax
NGC 1344	171.0 ± 8.0	1.210 ± 0.001	4.33 ± 0.15	2.14 ± 0.09	Fornax
NGC 1374	196.0 ± 9.0	1.214 ± 0.001	4.12 ± 0.13	1.56 ± 0.15	Fornax
NGC 1375	70.0 ± 9.0	1.195 ± 0.001	3.50 ± 0.23	2.93 ± 0.12	Fornax
NGC 1379	130.8 ± 8.2	1.197 ± 0.001	2.87 ± 0.19	1.68 ± 0.12	Fornax
NGC 1380	213.0 ± 6.0	1.206 ± 0.001	4.51 ± 0.10	1.70 ± 0.15	Fornax
NGC 1381	169.0 ± 8.0	1.208 ± 0.001	3.32 ± 0.15	1.63 ± 0.09	Fornax
NGC 1399	360.0 ± 8.0	1.204 ± 0.002	5.42 ± 0.23	1.29 ± 0.16	Fornax
NGC 1404	222.2 ± 7.7	1.216 ± 0.001	4.78 ± 0.08	1.46 ± 0.11	Fornax
NGC 1419	128.0 ± 6.0	1.198 ± 0.001	2.86 ± 0.17	1.62 ± 0.18	Fornax
NGC 1427	186.0 ± 11.0	1.201 ± 0.001	3.43 ± 0.17	1.58 ± 0.08	Fornax

For a relaxed system, i.e. a self-gravitating and stable, the velocity dispersion σ is a tracor of mass[7]. As

[7]See Appendix

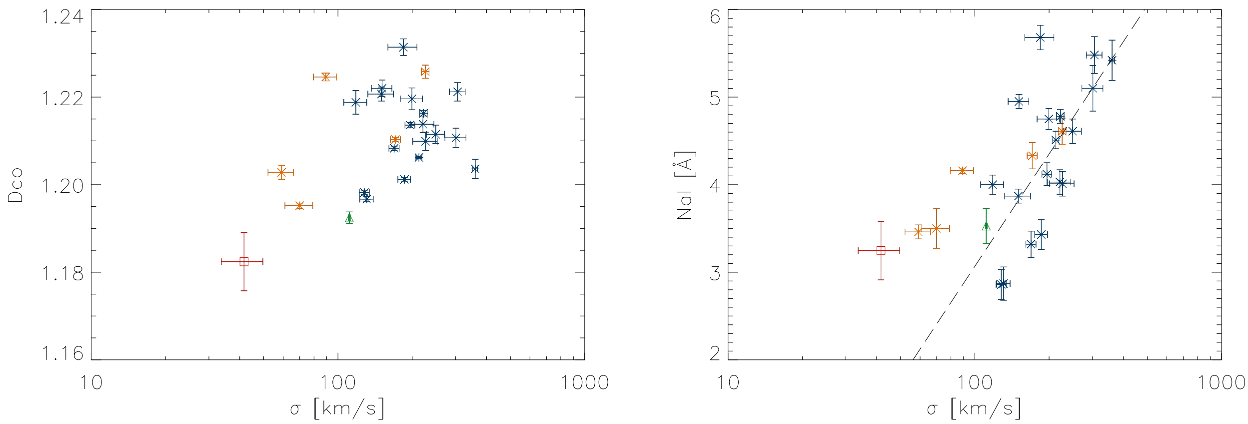

Figure 3.3.1: Coherence with galaxies belonging to the Fornax cluster . NGC 7252 [MEAN] is represented by a green triangle and W3 by a red square. The Fornax cluster galaxies with $H\beta \leq 2$ are in blue and in orange otherwise. The dashed line is a linear fit of the blue datapoints.

explained in Section (1.2.1), a massive galaxy should present higher metallicity. As the GCs come from a merger, a massive GC may show high metallicity as well. Finally, we should have a linear correlation between σ (in logarithmic scale) and all the metallicity indices : D_{CO}, CO and NaI. The center of NGC 7252 already presents a $R^{1/4}$ profile and has a single nucleus suggesting the merger is complete (Schweizer, 1982), we will then consider our targets as relaxed systems.

On Figure (3.3.1), we plotted two metallicity indicators as a function of σ. On the right panel, we have a tight correlation between the NaI index and σ as shown by the dashed line. $H\beta$ is one of the Balmer lines tracing hydrogen. A high $H\beta$ index indicates there are young stellar populations which contribute differently than the old ones. This is the reason why they don't follow the same correlation than those which present a lower index. On the D_{CO} plot, it seems there is not such correlation.

NGC 7252 nicely follows the correlation for NaI and also seems to be relevant among others early-type galaxies in the D_{CO} plot. However, we have not clear evidence for such tight correlation on the latter.

3.4 Comparison with the model

Let's compare now our results with the model using the Krupa IMF[8] from M05. In Table (3.3) are listed datapoints from L09a showing the marked disagreement. If we place all datapoints (from L09a and this project), we obtain Figure (3.4)

Table 3.3: K-Band indices in LMC GCs from L09a.

Name	Age [Gyr]	D_{CO}	NaI [Å]	CO [mag]
NGC 1754	10	1.082±0.005	0.14 ± 0.33	-0.035 ± 0.002
NGC 2005	10	1.086±0.003	0.34 ± 0.16	0.017 ± 0.001
NGC 2019	10	1.068±0.003	0.32 ± 0.25	-0.003 ± 0.001
NGC 1806	1.1	1.129±0.005	3.41 ± 0.32	0.026 ± 0.001
NGC 2162	2	1.108±0.010	3.37 ± 0.66	0.013 ± 0.002
NGC 2173	1.1	1.186±0.005	2.76 ± 0.29	0.123 ± 0.002

Regardless to the error estimations, Figure (3.4) seems to confirm the disagreement expected by L09b : both of our datapoints are far from the model on the CO-age plot, and again below it on the D_{CO}-age plot despite of a less marked disagreement. However, if we look closely, the results may not be as clear as we hope. Both model and our observations are not enough accurate to make a definite conclusion as discussed in Section (3.5).

[8]see Appendix

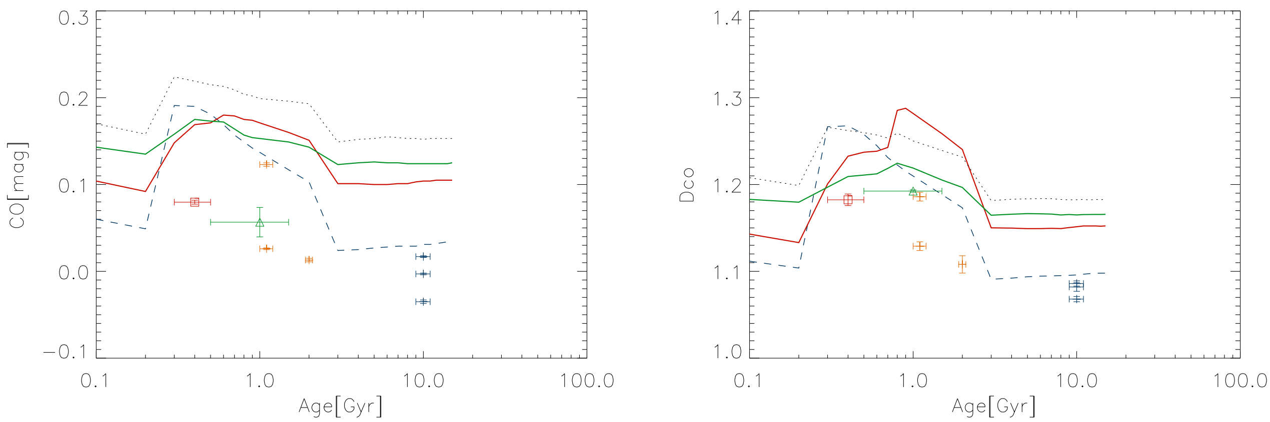

Figure 3.4.1: Comparison with the model. In blue and orange, previous datapoints from L09a. They must be compared with the dashed line ($0.05Z_{\odot}$) and the red solid line ($0.5Z_{\odot}$) respectively. In red, W3 and the model predictions for half solar metallicity. In green, NGC 7252 and the model for solar metallicity. Dotted line is the model for another metallicity.

3.5 Discussion

Our kinematics value for both NGC 7252 and W3 are consistent,within the error bars, with the previous literature values as presented in Chapter 1 except the velocity for NGC 7252 $v = 4754 \pm 2.2$ which is not in agreement with $v = 4828 \pm 3km.s^{-1}$ from Schweizer (1982). But, the previous value comes from a quite old study and derived from a visual spectrum which is highly influenced by the presence of dust. We can then assume our results are more reliable.

As any others early-type galaxies, we expected a gradient of metallicity, confirmed by the line strength gradient of the D_{CO} index. However, this index is influenced by, of course, the metallicity but also by the young stars. As NGC 7252 is a merger remnant, we don't know yet which exactly the stellar populations are involved. Therefore, any further interpretation is difficult.

In the near-IR index-σ scaling relations, NGC 7252 shows excellent consistency with others early type galaxies and follow a tight correlation for the NaI index. We may think that there is a correlation with the D_{CO} index but much more scattered probably because of the high dependence of the age of the stellar populations, unstudied so far. These characteristics are in agreement with the hierarchical galaxy formation scenario. Although W3 is considered as a GC throughout this report, the proximity of W3 with the others early-type galaxies in the indices-σ plot highlight the difficulty to clearly excludes it from being a galaxy (see Section (1.1.3)).

We turn now to the comparison of near-IR index measurements with model predictions. This project only focus on intermediate-age GCs, we will then not discuss the datapoints for $\sim 10\ Gyr$. As expected by L09b, both of the datapoints presented in this study show strong disagreement with the model. However, the measured CO values are not very accurate on the contrary of the model which benefits from the broad definition of the CO index. On the D_{CO} analysis, we have the contrary : the model, because of its low spectral resolution[9], suffers from the narrow definition of the D_{CO} index. Its predictions are therefore not as accurate as for the CO index. So even if the datapoints are still below the model, we have no evidence to confirm the previous result.

[9]one pixel covers 100Å

Chapter 4

Conclusions

1. We measured for NGC 7252 a recession velocity of $4754.5 \pm 2.7\ km.s^{-1}$ and a velocity dispersion of $111.3 \pm 1.0\ km.s^{-1}$, which is consistent with the previous measurements from Schweizer & Seitzer (1998). We show that this galaxy is rotating and is showing early-type characteristics : it follows the tight correlation between NaI index and σ and presents a metallicity gradient as function of radius.

2. About W3, we derived a recession velocity of $4776.7 \pm 5.2\ km.s^{-1}$ and an astonishing velocity dispersion of $41.6 \pm 8.0\ km.s^{-1}$, in excellent agreement with the previous analysis from Maraston et al. (2004). Moreover, its huge mass and its proximity in indices-σ plots is a hint that this object cannot be straightforward classified as a GC.

3. Finally, with this near-IR study, we have no clear evidence for confirming the disagreement expected by L09b because of the lack of accuracy in the data. It would be valuable to look into the datacube in order to improve the data reduction and then get more reliable measurements.

Chapter 5

Appendix

5.1 De Vaucouleur brightness profile

A good representation of the luminosity profile over many decades of surface brigthness is provided by the de Vaucouleurs law (5.1.1), usually referred to as the $r^{1/4}$ law.

$$log_{10}\frac{I(r)}{I(R_{eff})} = -3.3307\left[\left(\frac{r}{R_{eff}}\right)^{1/4} - 1\right] \tag{5.1.1}$$

This expression has been normalized so that R_{eff} (standing for effective radius) is the radius within which half the total luminosity is emitted and $I(R_{eff})$ is the surface brigthness at that radius.

5.2 Distance Modulus

The distance modulus is defined from the apparent magnitude m and the absolute magnitude M of a star. These quantities are defined by (5.2.1) and (5.2.2).

$$m = -2.5log_{10}(f) + C \tag{5.2.1}$$

$$M = -2.5log_{10}(F) + C \tag{5.2.2}$$

where C is an arbitrary constant set by choosing a star reference[1], defined by $m_0 = 0$. f is the observed flux at a distance d and F is the flux as seen by an observer at $D = 10pc$ from the star.

Assuming the total flux is conserved, we have the relation $\frac{f}{F} = \left(\frac{D}{d}\right)^2$ which leads to equation (5.2.3), relying immediatly the magnitude to the distance.

$$\boxed{m - M = 5log_{10}\left(\frac{d}{D}\right)} \tag{5.2.3}$$

Note that in many applications, we refer only to the distance modulus of different objects rather than converting back to the distances in parsecs or lightyears. From this definition, two different kind of distance modulus can be calculated : the visual apparent distance modulus $(m - M)_0$ where the absolute magnitude has been estimated by theory and the true distance modulus $V - M_V$ which calculate M in a finer manner by taking into account the interstellar absorption coefficient.

5.3 Mass-velocity dispersion relation

For a system in statistical equilibrium, we have the well-known virial theorem (5.3.1) relating the total kinetic energy T to the gravitational potential energy U.

$$2T + U = 0 \tag{5.3.1}$$

[1] Usually Vega

If we assume that the velocity distribution in the system is isotropic (e.g. in a globular cluster or an elliptical galaxy), the same velocity dispersion is expected in any spatial direction such as $\langle v^2 \rangle = \langle 3v_{LOS}^2 \rangle$ where $\langle v \rangle$ is the absolute velocity dispersion and $\langle v_{LOS} \rangle$ is the velocity dispersion along the Line Of Sight. We have then $T = \frac{1}{2}M\langle v^2 \rangle = \frac{3}{2}M\langle v_{LOS}^2 \rangle$. If the velocity dispersion varies with mass, then $\langle v_{LOS} \rangle$ is a mass-weighted velocity dispersion. If the system is also spherically symmetric, we can suitably define a weighted mean separation R between each star. So that, we can derive a mass-velocity dispersion relation from the virial theorem (see Equation (5.3.2)).

$$\begin{cases} U = -\dfrac{GM^2}{R} \\ T = \dfrac{3}{2}M\langle v_{LOS}^2 \rangle \end{cases}$$
$$\Leftrightarrow M = \frac{3\langle v_{LOS}^2 \rangle R}{G} \tag{5.3.2}$$

We want to point out that the mass M of a system in equilibrium is related to the mesured (along the line of sight) velocity dispersion σ_v such as $\boxed{M \propto \sigma_v^2}$

5.4 Initial Mass Function (IMF)

The entire evolution of a star is determining by their initial mass. It is now an accepted fact that stars form by groups from a gaz cloud. The IMF $\xi(M)$ is an empirical function that describes the mass distribution of a population of stars. The first IMF was quantified by Salpeter 1955 and shows that the number of stars decreases rapidly with mass (see Equation (5.4.1)). In this report, we will assume another more recent IMF called the Krupa IMF given by relation (5.4.2).

$$\xi(M) = \xi_0 M^{-2.35} \tag{5.4.1}$$

$$\xi(M) = \begin{cases} 0.93M^{0.15} & 0.1 \leq M \leq 0.5 \\ 0.46M^{-0.85} & 0.5 \leq M \leq 1.0 \\ 0.46M^{-2.4} & 1.0 \leq M \leq 3.16 \\ 0.21M^{-1.7} & 3.16 \leq M \leq 100 \end{cases} \tag{5.4.2}$$

Where M is the mass of star in solar mass $M_\odot$.

However, these laws are still in a debate we will not discuss.

Bibliography

Anderson A. J., 1997, PhD thesis, AA(UNIVERSITY OF CALIFORNIA, BERKELEY)

Bedin L. R., Piotto G., Anderson J., Cassisi S., King I. R., Momany Y., Carraro G., 2004, ApJL, 605, L125

Cappellari M., Copin Y., 2003, MNRAS, 342, 345

Cappellari M., Emsellem E., 2004, PASP, 116, 138

Cassisi S., Castellani V., Degl'Innocenti S., Piotto G., Salaris M., 2001, A&A, 366, 578

Faber S. M., Friel E. D., Burstein D., Gaskell C. M., 1985, ApJS, 57, 711

Frogel J. A., Stephens A., Ramírez S., DePoy D. L., 2001, AJ, 122, 1896

Kormendy J., Bender R., 1996, ApJL, 464, L119+

Kuntschner H., 2000, MNRAS, 315, 184

Larsen S. S., Brodie J. P., Hunter D. A., 2004, AJ, 128, 2295

Lyubenova M., 2009a, A&A, "Submitted"

—, 2009b, PhD thesis, Ludwig-Maximilians-Universitat

M. J., C. J. A. R., 1936, Science, 84, 509

Maraston C., 2005, MNRAS, 362, 799

Maraston C., Bastian N., Saglia R. P., Kissler-Patig M., Schweizer F., Goudfrooij P., 2004, A&A, 416, 467

Maraston C., Kissler-Patig M., Brodie J. P., Barmby P., Huchra J. P., 2001, A&A, 370, 176

Mármol-Queraltó E., 2009, ApJ, "Submitted"

Mármol-Queraltó E., Cardiel N., Cenarro A. J., Vazdekis A., Gorgas J., Pedraz S., Peletier R. F., Sánchez-Blázquez P., 2008, A&A, 489, 885

Renzini A., 1998, AJ, 115, 2459

Schweizer F., 1982, ApJ, 252, 455

Schweizer F., Seitzer P., 1998, AJ, 116, 2206

Silva D. R., Kuntschner H., Lyubenova M., 2008, ApJ, 674, 194

Toomre A., Toomre J., 1973, Scientific American, 229, 38

Trager S. C., Worthey G., Faber S. M., Burstein D., Gonzalez J. J., 1998, ApJS, 116, 1

Worthey G., Faber S. M., Gonzalez J. J., Burstein D., 1994, ApJS, 94, 687

Zhang Q., Fall S. M., 1999, ApJL, 527, L81